Materials Research Letters

ISSN: 2166-3831 (Online) Journal homepage: www.tandfonline.com/journals/tmrl20

Hierarchically heterogeneous microstructure and mechanical behavior of the multi-materials prepared by powder severe plastic deformation

Sujung Son, Jungwan Lee, Peyman Asghari-Rad, Rae Eon Kim, Hyojin Park, Jae-il Jang, Wen Chen, Yoon-Uk Heo & Hyoung Seop Kim

To cite this article: Sujung Son, Jungwan Lee, Peyman Asghari-Rad, Rae Eon Kim, Hyojin Park, Jae-il Jang, Wen Chen, Yoon-Uk Heo & Hyoung Seop Kim (2023) Hierarchically heterogeneous microstructure and mechanical behavior of the multi-materials prepared by powder severe plastic deformation, Materials Research Letters, 11:11, 915-924, DOI: 10.1080/21663831.2023.2258158

To link to this article: https://doi.org/10.1080/21663831.2023.2258158

© 2023 The Author(s). Published by Informa UK Limited, trading as Taylor & Francis Group.

View supplementary material

Published online: 19 Sep 2023.

Submit your article to this journal

Article views: 2636

View related articles

View Crossmark data

Citing articles: 13 View citing articles

Full Terms & Conditions of access and use can be found at
https://www.tandfonline.com/action/journalInformation?journalCode=tmrl20

MATER. RES. LETT.
2023, VOL. 11, NO. 11, 915–924
https://doi.org/10.1080/21663831.2023.2258158

ORIGINAL REPORTS

OPEN ACCESS

Hierarchically heterogeneous microstructure and mechanical behavior of the multi-materials prepared by powder severe plastic deformation

Sujung Son [a], Jungwan Lee [a], Peyman Asghari-Rad [a], Rae Eon Kim [b], Hyojin Park [a], Jae-il Jang [c], Wen Chen [d], Yoon-Uk Heo [b] and Hyoung Seop Kim [a,b,e,f]

[a]Department of Materials Science and Engineering, Pohang University of Science and Technology (POSTECH), Pohang, Republic of Korea; [b]Graduate Institute of Ferrous & Eco Materials Technology, Pohang University of Science and Technology (POSTECH), Pohang, Republic of Korea; [c]Division of Materials Science and Engineering, Hanyang University, Seoul, Republic of Korea; [d]Department of Mechanical and Industrial Engineering, University of Massachusetts, Amherst, MA, USA; [e]Advanced Institute for Materials Research (WPI-AIMR), Tohoku University, Sendai, Japan; [f]Institute for Convergence Research and Education in Advanced Technology, Yonsei University, Seoul, Republic of Korea

ABSTRACT

A heterostructuring strategy is an effective approach for abiding problems referred to as the strength-ductility trade-off. However, tailoring the heterostructure is an arduous problem. This work synthesized hierarchically heterogeneity by combining the eutectic high-entropy alloy (EHEA) and medium-entropy alloy powders through novel powder metallurgy-based severe plastic deformation (P-SPD). EHEA forms nano-scaled heterogeneity composed of FCC and B2, and the mixture of powder types forms micro-scale heterogeneity with hard and soft domains. This hierarchically heterogeneous microstructure leads to strong hetero-deformation-induced strengthening, achieving a yield strength of ∼ 1.5 GPa. The present P-SPD represents the feasibility of heterostructuring, aiding the development of HEAs.

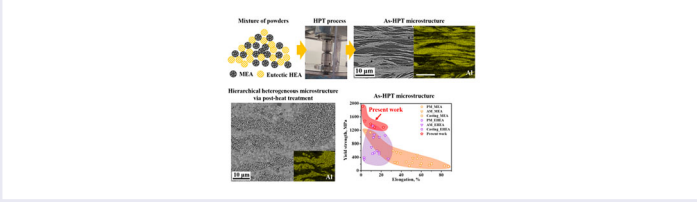

IMPACT STATEMENT

A hierarchically heterogeneous microstructure comprised of the eutectic high-entropy alloy and medium-entropy alloy was synthesized by the P-SPD procedures and achieved supreme mechanical properties attributed by hetero-deformation-induced strengthening.

ARTICLE HISTORY
Received 20 May 2023

KEYWORDS
High-entropy alloys; high-pressure torsion; multi-materials; heterostructures; mechanical properties

Introduction

Achieving a combination of high strength and ductility has been pursued by numerous metallurgists. Diverse strategies such as alloy design, severe plastic deformation (SPD), and heat treatment have been attempted. In considering the developing materials, the homogeneous structures have been deemed optimized microstructures to avoid early fracture initiation at the domain boundaries in the heterogeneous materials. However, the advantages of heterostructuring to achieve high strength and reasonable ductility are emerging recently [1–4]. Several studies reported synergetic strengthening to overcome the strength-ductility trade-off in heterostructures, such as harmonic, sandwich, gradient, and layered structures [5–7]. However, tailoring heterostructures in the microscale as intended is still problematic.

Powder metallurgy (PM) is a facile manufacturing method combining various powders, such as metals, alloys, ceramics, and polymers [8]. The heterostructure on a microscale can be manufactured by combining

CONTACT Hyoung Seop Kim hskim@postech.ac.kr Department of Materials Science and Engineering, Pohang University of Science and Technology (POSTECH), 37673, Pohang, Republic of Korea; Graduate Institute of Ferrous and Energy Materials Technology, Pohang University of Science and Technology (POSTECH), 37673, Pohang, Republic of Korea; Advanced Institute for Materials Research (WPI-AIMR), Tohoku University, 980-8577, Sendai, Japan; Institute for Convergence Research and Education in Advanced Technology, Yonsei University, 03722, Seoul, Republic of Korea; Peyman Asghari-Rad peyman.asghari.rad@gmail.com Department of Materials Science and Engineering, Pohang University of Science and Technology (POSTECH), 37673, Pohang, Republic of Korea

Supplemental data for this article can be accessed here. https://doi.org/10.1080/21663831.2023.2258158

© 2023 The Author(s). Published by Informa UK Limited, trading as Taylor & Francis Group.
This is an Open Access article distributed under the terms of the Creative Commons Attribution License (http://creativecommons.org/licenses/by/4.0/), which permits unrestricted use, distribution, and reproduction in any medium, provided the original work is properly cited. The terms on which this article has been published allow the posting of the Accepted Manuscript in a repository by the author(s) or with their consent.

different types of powders. However, PM-processed parts usually lack ductility under tension because of pores, contaminations, and undesired phases formed during mechanical alloying and high-temperature sintering [9,10]. A novel PM-based fabrication route densifies powders through the high-pressure torsion (HPT) process at ambient temperature, leading to the utmost densification [11,12]. Furthermore, the HPT process is a well-known SPD technique, fabricating nano/ultrafine-grained materials [13–16].

In this work, heterogeneous multi-materials with medium-entropy alloy (MEA) and eutectic high-entropy alloy (EHEA) are fabricated through the abovementioned PM-based technique. As a single material, the achievable mechanical properties of MEA are limited. And, EHEA powder is too hard to be pre-compacted in powder metallurgy. Therefore, the mixture of MEA and EHEA can lead to a complementary relationship. EHEA acts as a reinforcement material in MEA and MEA acts as a binder material in EHEA. Consequently, hierarchically heterogeneous microstructure and exceptional mechanical properties of MEA-EHEA multi-materials were systematically investigated.

Materials and methods

The CoCrFeNi MEA and $AlCoCrFeNi_{2.1}$ EHEA powders were fabricated using gas atomization. The produced powders were mixed in proportions targeting the 50 at% of MEA and EHEA. The powders were pre-compacted at a pressure of 40 MPa to manufacture a disk-shape sample with a diameter of 10 mm and a thickness of 1.2 mm. The pre-compacted disks were subjected to the HPT process with a pressure of 5 GPa for 4 turns at a rate of 1 rpm. Then, the HPT-processed samples with a thickness of 0.8 mm were annealed at 700 and 800 °C for 15 and 60 min under an Ar atmosphere. The HPT-processed and post-HPT annealed samples were denoted as As-HPT, A715, A760, A815, and A860, respectively, according to the annealing temperature and time.

For microstructural analysis, X-ray diffraction (XRD), scanning transmission electron microscope (STEM) and scanning electron microscopy (SEM) with backscatter electron (BSE), energy-dispersive spectroscopy (EDS), and electron backscatter diffraction (EBSD) detectors were utilized. Furthermore, the synchrotron XRD characterization was conducted at the 8D beamline of the Pohang Accelerator Lab. Tensile tests and loading-unloading-reloading (LUR) tests were performed on the dog-bone-shaped samples with a gauge length of 1.5 mm, a thickness of 0.8 mm, and a width of 0.7 mm. The quasi-static strain rate of 10^{-3} s^{-1} was used for the mechanical tests. A precise tensile strain was taken by a digital image correlation (DIC) method.

Results and discussion

In Figure 1(a-d), the BSE micrographs and EDS maps are obtained in the spherical-shaped gas-atomized MEA and EHEA powders. There is no elemental segregation in the MEA powder (Figure 1(b)), while the phase separation between the Al-rich phase and Al-lean phase is observed in the EHEA powder (Figure 1(d)). In $AlCoCrFeNi_{2.1}$ EHEA, the phase separation from liquid to Al-lean face-centered cubic (FCC) and Al-rich B2 structures is reported at below ~1320 °C [17]. Figure 1(e) exhibits an overall cross-section of the as-HPT sample with a defect-free structure. In detail, the magnified microstructure of the as-HPT sample displays two domains elongated along the HPT rotation direction (Figure 1(f)). The corresponding EDS maps in Figure 1(g) exhibit the Al-lean MEA and Al-rich EHEA domains. Due to severe friction stress during the HPT process, the interfaces between MEA and EHEA powders are strongly bonded [11]. The EDS line profile across the domain interface is shown in Fig. S1. According to the distribution of Al, the diffusion layer formed during the HPT process is less than 1 μm. Notably, the EHEA domain in the as-HPT sample presents a segregation-free structure, unlike the starting EHEA powder. To distinguish nano-scaled elemental segregation, STEM analysis was performed. Figure 1(h) exhibits a sound interface between the MEA and EHEA domains without bonding defects. The SAED rings of both domains are obtained from the selected regions (yellow region: MEA and red region: EHEA). The SAED rings of the MEA domain indicate that the FCC structure remains after the HPT process. Similarly, SAED rings of the FCC phase are detected in the EHEA domain. The fast Fourier transform (FFT) patterns from MEA and EHEA also exhibit FCC structures (Figure 1(i, j)). In other words, the B2 phase observed in starting EHEA powder (Figure 1(c, d)) disappears after the HPT processing, attributable to the dissolution of B2 phase under SPD [18–20]. From the diameter of SAED rings, the lattice parameters of the FCC phase in the MEA and EHEA are calculated as 3.55 and 3.59 Å, respectively. The dissolution of the B2 phase could be inferred by the decreased diameter of SAED rings in EHEA compared to MEA. The penetration of Al elements in the FCC matrix by the dissolution of B2 phase leads the larger lattice parameters, shrinking the SAED rings. In addition, the MEA and EHEA domains are refined as a nanocrystalline microstructure by the HPT process. The magnified HR-TEM images of the MEA and EHEA domains exhibit ultrafine-grained structures in Fig. S2. The grain sizes of the MEA and EHEA are ~29.4 and ~25.3 nm, respectively.

XRD spectra of all samples shown in Figure 2(a) are consistent with the HR-TEM results. Initial MEA

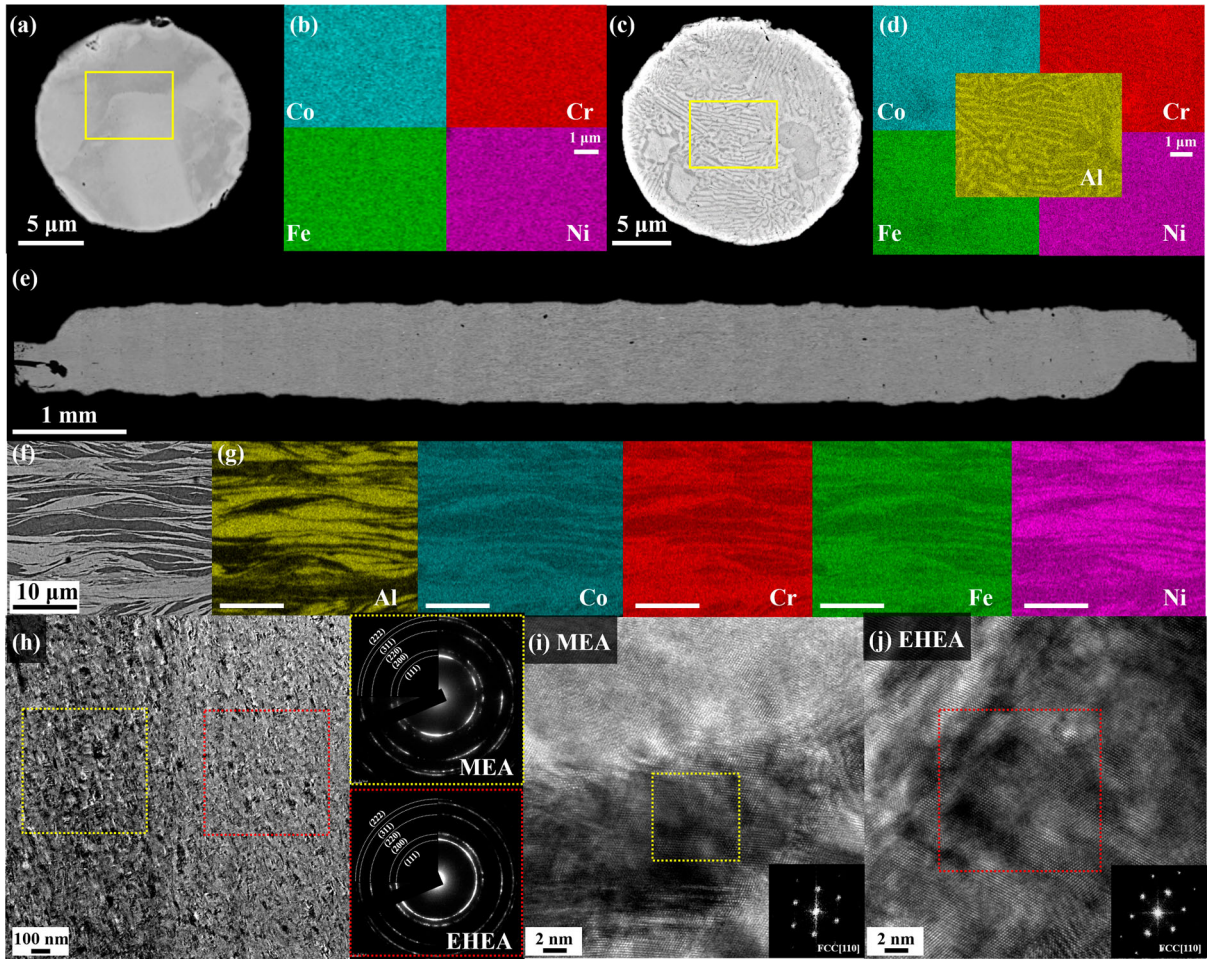

Figure 1. (a, c) SEM-BSE micrographs and (b, d) EDS maps of the gas-atomized (a, b) MEA powder and (c, d) EHEA powder, (e) the cross-section SEM image of the As-HPT sample, (f) SEM-BSE image of the As-HPT sample with (g) corresponding EDS maps, (h) bright field TEM micrographs of the MEA/EHEA interface with SAED ring patterns from MEA and EHEA regions, and HR-TEM micrographs of MEA and EHEA is shown in (i) and (j) accompanied by FFT patterns, respectively.

powders contain FCC single-phase, and EHEA powders consist of FCC and B2 dual-phase (Figure 2(a)). However, the peaks related to the B2 phase are not detected in the spectrum of the as-HPT sample, owing form the dissolution of B2 phase under severe HPT-induced strain. Subsequent annealing on the HPT-processed samples is conducted to tailor the microstructure to reach a good combination of strength and ductility. The phase decomposition to FCC and B2 phase occurs in all annealed samples according to the B2 peaks detected at 2theta of ~ 82°. After HPT processing, the dissolution of B2 makes a supersaturated FCC phase in the EHEA which is thermodynamically unstable [21]. Also, the diffusion process is generally accelerated in severely deformed alloys due to lattice defects [22]. Therefore, the post-HPT annealing, even for a short time, leads to the decomposition of the supersaturated FCC matrix in the EHEA domains. To verify the recrystallization behavior, EBSD and convolutional multiple whole profile (CMWP) analyses were performed on the A715 sample (Fig. S3). Even with the lowest annealing temperature and shortest annealing time, the A715 sample exhibitsed a low average KAM value of ~ 0.32° and dislocation density of 8.77×10^{13} m^{-2}, as determined from CMWP fitting, indicating a fully recrystallized microstructure [23].

The distribution of the constituent phases is displayed in Figure 2(b, c). The MEA and EHEA domains are distinguished by the enveloped Al element maps. And, EDS line profiles of A715 and A860 samples are shown in Figure 2(d, e). The fluctuations of elemental distribution are observed in the EHEA domain because of the phase separation to FCC and B2 phases. Between EHEA and MEA domains, the diffusion layers are extended over 1 µm after annealing. Interestingly, the presence of Al over 3 at% is observed in MEA domains, which indicates some EHEA domains dissolved in MEA domains rather than forming separated EHEA domains. The compositions of the domains were summarized in Table S1. The

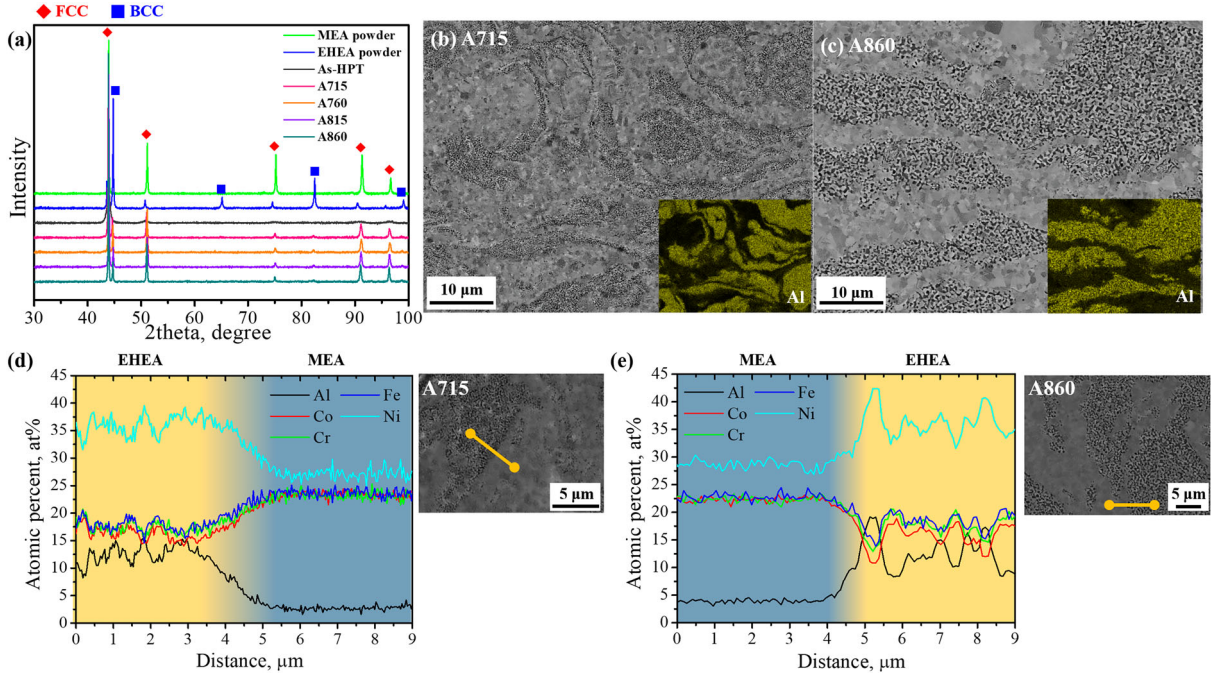

Figure 2. (a) X-ray diffraction patterns of the powders, as-HPT sample, and annealed samples at different temperatures and times, SEM-BSE micrographs of the (b) A715 and (c) A860 samples, and (d, e) EDS line profiles obtained from the yellow lines indicated in the enveloped BSE images.

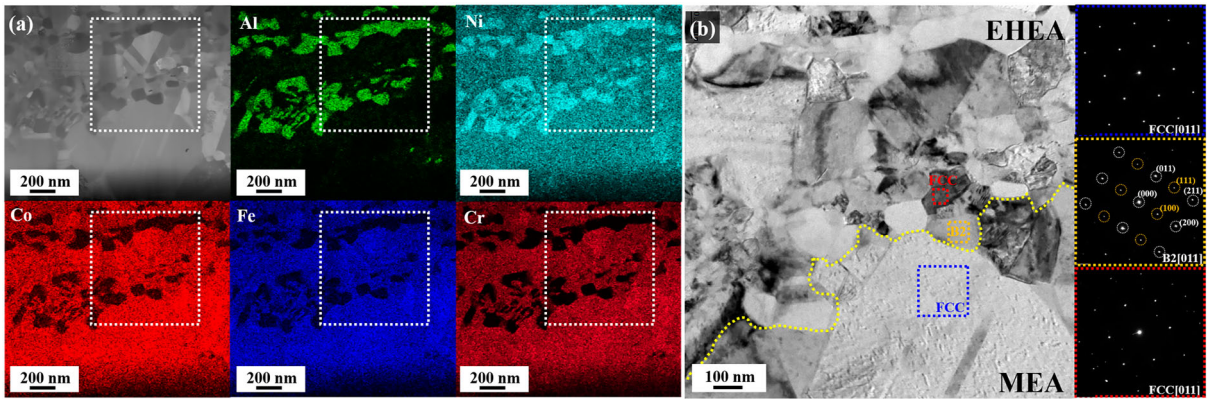

Figure 3. (a) TEM micrographs of the interface of the MEA and EHEA domains with the corresponding EDS maps and (b) HRTEM images with the FFT patterns of FCC and B2 phases in A715.

increased contents of Ni in MEA domains also support the dissolution of EHEA domains in MEA domains.

In Figure 3, TEM micrographs and corresponding EDS maps of the domain interfaces in the A715 sample show the decomposition of the EHEA to the Al-rich and Al-lean regions. From the FFT pattern obtained in the HR-TEM image, the Al-rich and Al-lean regions are confirmed to be the B2 and FCC phases.

Since the EHEA domain decomposes to a dual-phase structure during the post-HPT annealing, the grain growth is retarded in this domain because one phase can effectively resist the growth of the other phase, resulting in the finer grain size [22,24]. As a result, the FCC grains in the EHEA domain contain a finer grain size of ~463 nm than the FCC grains in the MEA domain of ~778 nm in the A715 sample. Also, the grain size of the B2 phase (~393 nm) is similar to the FCC grain size in the EHEA. In the A860 sample, as the annealing temperature and time increase, the grain size increases in both MEA and EHEA domains. However, the difference in the grain size gets distinctly in the A860 sample. The FCC grain size in the MEA grows up to ~1.282 μm, while the grain size of FCC and B2 phases in the EHEA remains about ~400 nm. Consequently, a hierarchically heterogeneous structure is achieved, containing coarse FCC grains in the MEA domain, and fine FCC and B2 grains in the EHEA domain. Furthermore, the nanoindentation hardness of each phase is reported as 9.7 (B2),

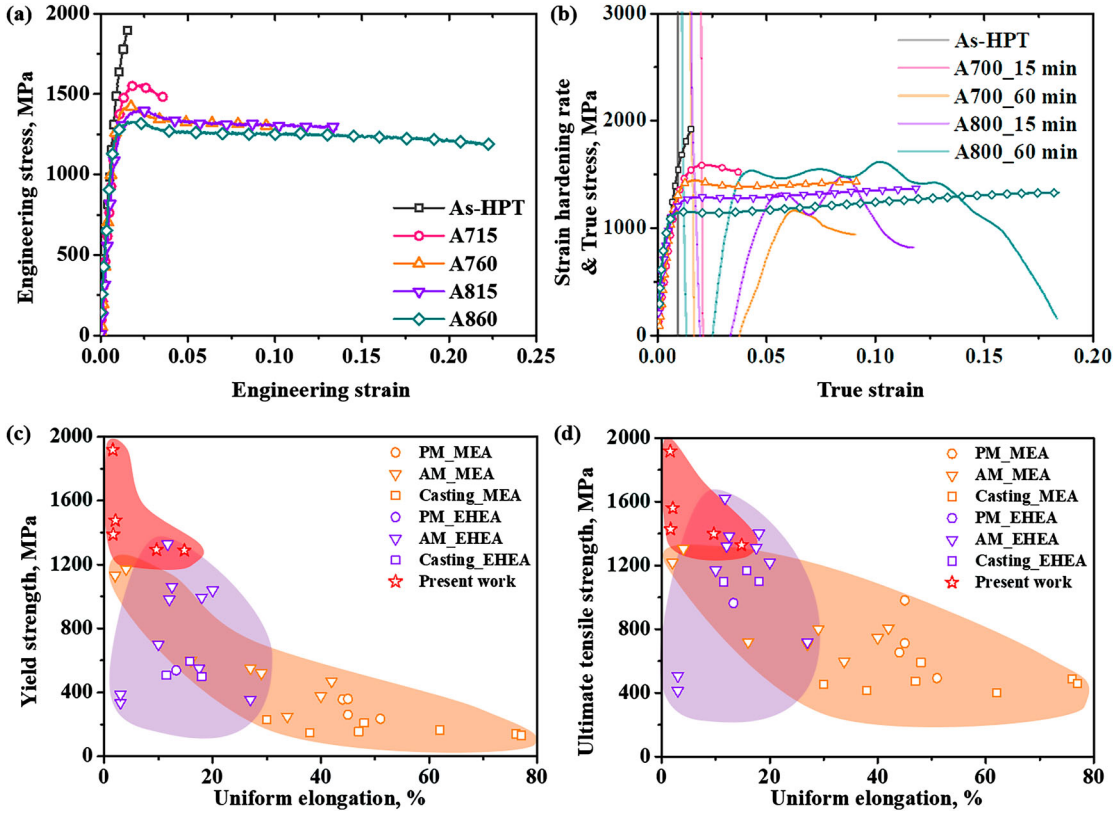

Figure 4. (a) Engineering stress-strain curves of the as-HPT and annealed samples, (b) SHR curves. Comparison of (c) YS vs. uniform elongation and (d) UTS vs. uniform elongation of the samples in the present work and literature processed by the casting, conventional powder metallurgy (PM) routes, and additive manufacturing (AM) [12,38–52].

5.8 (FCC in the EHEA domain), and 4.6 GPa (MEA), respectively [25,26]. Because the B2 and FCC phases in the EHEA domain have higher hardness and finer grain size, the difference in mechanical properties between the MEA and EHEA domains become more pronounced. The present hierarchically heterogeneous structure consists of grain size heterogeneity in FCC grains, chemical composition heterogeneity stemming from different powders, and crystal structure heterogeneity originating from phase decomposition to FCC and B2 phases.

The tensile stress-strain curves are displayed in Figure 4(a). The tensile strength of the as-HPT sample reaches ~1.92 GPa, representing the strong bonding between different powders achieved by cold-consolidation using P-SPD procedure. Due to the restricted dislocation movement in the as-HPT sample, this sample demonstrates a limited plastic deformation [12,27]. After the post-HPT annealing, the ductility is improved in the cost of strength. The yield strength (YS) values of the annealed samples decrease from ~1476 (A715), ~1388 (A760), ~1293 (A815), to ~1289 MPa (A860) due to the reduced dislocation density and grain growth, while total elongation continuously increases from ~4% (A715), ~10 (A760), ~14 (A815), to 22% (A860). Noticeably, all annealed samples exhibit remarkable YS over 1.2 GPa, attributing to the nano-crystalline microstructure, utmost densification, high dislocation density, strong B2 phases, and hierarchical heterostructure achieved by the present fabrication technique.

To clarify the source of high YS, the expected YS is calculated using the rule of mixture (ROM) equation [28]. The A860 sample consists of MEA and EHEA domain with an atomic percent of 50%, which can be recalculated to 49.4 Vol% of MEA and 50.6 Vol% of EHEA using the atomic weight of constituent elements and density of alloys. First, the strength of the MEA domain is obtained from the following Hall-Petch equation [29]:

$$\sigma_{MEA} = \sigma_{0_MEA} + K_{MEA} \cdot d^{-\frac{1}{2}}, \tag{1}$$

where σ_{MEA}, σ_{0_MEA}, K_{MEA}, and d are YS, friction stress (256 MPa), Hall-Petch coefficient (226 MPa $\cdot$ $\mu m^{\frac{1}{2}}$), and grain size of MEA domain, respectively [30]. By substituting the grain size of the A860 sample (~1.3 μm) into the equation, the YS of the MEA domain is calculated as ~454 MPa.

Meanwhile, the Hall-Petch-type equation can be used in the EHEA [31]:

$$\sigma_{EHEA} = \sigma_{0_EHEA} + K_{EHEA} \cdot \lambda^{-\frac{1}{2}}, \tag{2}$$

where σ_{EHEA}, σ_{0_EHEA}, K_{EHEA}, and λ are YS, friction stress, Hall-Petch coefficient, and inter-lamellar spacing of the EHEA domain. The inter-lamellar spacing ($\sim$0.86 μm) is calculated as the sum of grain sizes of FCC and B2 phases in the EHEA domain. The σ_{0_EHEA} and K_{EHEA} are obtained as 163 MPa and 907 MPa $\cdot\ \mu m^{\frac{1}{2}}$, by plotting the data of YS and inter-lamellar spacing in Ref. [32]. The YS of the EHEA domain is calculated as $\sim$1142 MPa. Using ROM equation, the YS of MEA-EHEA multi-materials is predicted to be 802 MPa, which cannot represent the experimental YS. The difference between the calculated and experimental YS is assumed to be attributed to residual stress, dislocations, contamination of powders, and HDI strengthening. Furthermore, the large Al atoms added to MEA domains during the annealing process can induce additional solid solution strengthening [3]. The microstructural heterogeneity could induce massive plastic incompatibility between the domains. To maintain plastic compatibility, geometrically necessary dislocations (GNDs) could be generated and piled up at the domain boundaries, leading to heterodeformation induced (HDI) strengthening [33–35]. The HDI strengthening contributes to YS and additional strain hardening, resulting in a good combination of strength and ductility [3,33,34].

Meanwhile, it is known that post-elongation after necking can be affected by the sample dimension, while the uniform elongation before necking is independent of sample thickness and gauge length [36]. To exclude the sample size effects, the uniform elongation is determined from the intersection of true stress–strain curves and strain-hardening rate (SHR) curves in Figure 4(b). To obtain the uniform elongation and valuate the contribution of HDI strengthening, the strain-hardening behaviors of the samples are examined using the strain-hardening rate (SHR) curves in Figure 4(b). The as-HPT sample shows a decreasing trend in SHR until fracture. This behavior is usually observed in SPD materials with high dislocation density [27]. Meanwhile, the SHR curves of the annealed samples show dramatic drops under subzero values after yielding, which was observed in ultrafine-grained materials due to the yield drop phenomenon [12]. Then, the SHR values of the A760, A815, and A860 samples return to positive and fluctuate in positive values until fracture. The different domain sizes for GND accumulation and the saturation of dislocation at different strain levels lead to the fluctuation of the SHR values. Among the intersection of the true stress–strain curves and the SHR curves, the highest strain is considered the onset of necking [37]. The uniform elongation increases from $\sim$2% (A715), $\sim$2% (A760), $\sim$10% (A815), to 15% (A860). With controllable annealing, an exceptional strength-ductility combination of YS $\sim$1289 MPa and uniform elongation $\sim$15% is obtained in the A860 sample.

The YS vs. uniform elongation and the ultimate tensile strength (UTS) vs. uniform elongation of the samples in this study are compared to those of the MEAs and EHEAs from literature (Figure 4(c, d)) [12,38–52]. To exclude the size effect, the values of uniform elongation were used for comparison. The multi-materials fabricated in this study exhibit superior mechanical properties to all MEAs in the previous studies. Moreover, the strength of multi-materials is higher or similar to that of EHEAs fabricated by casting, powder metallurgy, and additive manufacturing. Considering the simple calculation from the ROM [28], the mechanical properties of this study should be positioned in the intermediate range of the MEAs and EHEAs. However, the mechanical properties of these multi-materials are placed above the those of single EHEAs and MEAs. The impressive mechanical properties achieved in this study are attributed to grain refinement, dislocation density, and heterostructures, which can be manufactured by the novel P-SPD technique. Furthermore, superior mechanical properties would be expected by controlling the ratio of powders and adding reinforcement particles to fabricate HEA/MEA-matrix composites.

To evaluate the contribution of HDI strengthening in the present hierarchically heterostructure, the ratios of HDI stress to flow stress are calculated at different true strains from the LUR test of the A860 sample (Figure 5(a,b)). The HDI stress and effective stress of the sample are summarized in Table S2. The effective stress of the A860 remains around 500 MPa, while the values of HDI stress steadily increase from $\sim$637 to $\sim$802 MPa. Also, the strain hardening of the A860 sample is predominantly attributed to HDI stress, which occupies $\sim$60% of flow stress.

Figure 5(c-e) and Figure 5(f-h) represent the phase maps and KAM maps of the A860 sample in the different local strains to assess the evolution of GNDs in the present hierarchically heterostructure. The KAM evolutions in the MEA and EHEA domains at the different local strains are summarized in Fig. S4. The initial microstructures are obtained in the grip part of the tensile sample, which exhibits a low level of KAM values. The low KAM value means that the HPT-induced dislocations are recovered during annealing. Meanwhile, at the local strain of $\sim$0.15 (Figure 5(d,g)), the KAM values of the FCC phases (0.50°) in the EHEA domain increase first, owing to profuse phase boundaries between FCC and B2 phases. The hard B2 phase and soft FCC matrix in the EHEA develop GNDs to maintain strain compatibility [33,53]. Ultrafine grains of FCC and B2 phases in the EHEA domains offer profuse grain boundaries

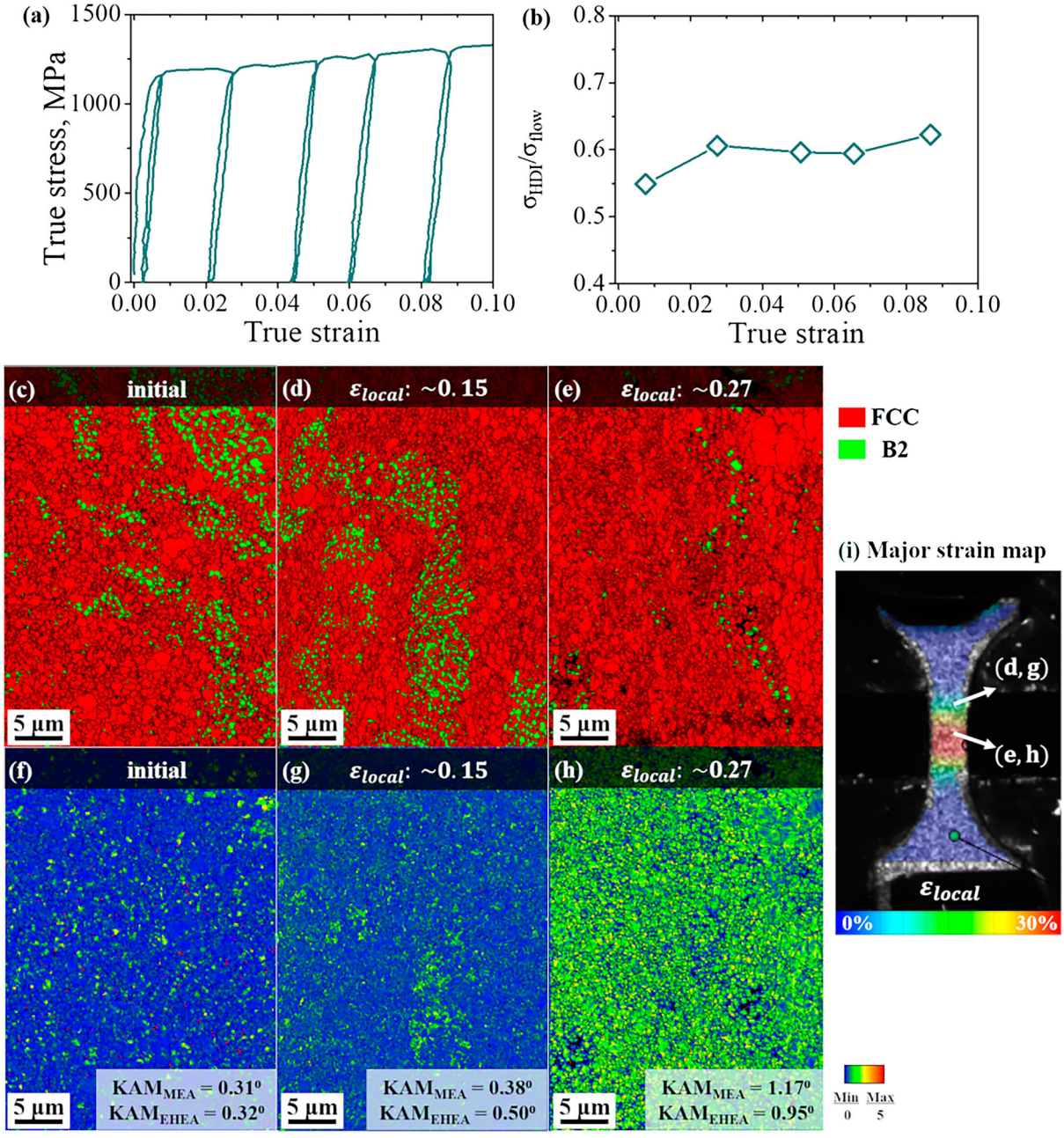

Figure 5. (a) Loading-unloading-reloading curves of the A860, (b) ratio of HDI stress to flow stress taken from the LUR test, and (c-h) EBSD-KAM maps taken from (i) the major strain map of the deformed A860 sample at (c, f) an initial state and local strain of (d, g) ~ 0.15 and (e, h) 0.27, respectively. The KAM maps are measured up to the third nearest neighbor with a maximum misorientation of 5°.

and phase boundaries. Furthermore, the B2 phases act as strong obstacles to dislocation movement [45]. Abundant obstacles like the B2 phase, phase boundaries, and grain boundaries attribute the steep increase of dislocation density in the FCC phases of EHEA domains. However, the dislocation accumulation shows a different aspect in the intensely deformed microstructures at the local strain of ~0.27 (Figure 5(e,h)). The KAM value of the MEA domain (1.17°) increased significantly, surpassing the KAM value of the FCC in the EHEA domain (0.95°). Because the EHEA domains act as hard domains, and the MEA domains act as soft domains in the microscale, the GND evolves in the MEA domains to compensate for the strain incompatibility, leading to an additional HDI strengthening.

Those KAM evolutions displayed in Figure 5(c-h) can help elucidate the trend of the ratio of HDI stress to flow stress in Figure 5(b). The microstructural inhomogeneity between the FCC and B2 phases in the EHEA is repeated at the nanoscale, leading to a rapid increase

and subsequent saturation of dislocation density. The ratio of HDI stress to flow stress sharply increases from 0.55 ($\epsilon_{true} = 0.01$) to 0.61 ($\epsilon_{true} = 0.03$), which can be attributed to the increased accumulation of GNDs within the EHEA domain. On the other hand, the MEA and EHEA domains repeat at the in microscale, resulting in a relatively slower increase in the ratio of HDI stress to flow stress.

Conclusion

While the importance and expediency of the heterostructuring are getting more and more attention, it is noteworthy that a hierarchical heterostructuring can be obtained by selecting appropriate materials and consolidating their powder mixtures. In this work, a sound bulk disk with hierarchically heterogeneous structures was fabricated by combining the ductile CoCrFeNi MEA and hard $AlCoCrFeNi_{2.1}$ EHEA powders with a dual-phase structure. HPT processing and adequate heat treatment led this multi-material to have a hierarchically heterogeneous structure, consisting of (1) nano-scaled phase separation within EHEA and (2) EHEA-MEA domain separation, leading to a superior combination of mechanical strength and ductility compared to EHEA and MEA of the previous studies. Furthermore, the ultrafine grains fabricated by SPD process effectively improved the strength of multi-materials. These materials could be considered in high-tech applications such as micro-gears. This study suggests an attractive solution to the fabrication of hierarchically heterogeneous structures, which have been considered troublesome. A complicated heterostructure with two or more hierarchies can be fabricated by including several powders of various physical properties, combining powders with heterostructures, or controlling the powder size and powder ratio. The suggested solution for the hierarchically heterogeneous structuring would be a breakthrough to achieve supremum properties through a PM-based technique.

Acknowledgments

We thank Prof. Byeong-Joo Lee from POSTECH for helping us with the thermodynamic calculations.

Disclosure statement

No potential conflict of interest was reported by the author(s).

Funding

This work was supported by the Nano & Material Technology Development Program through the National Research Foundation of Korea funded by Ministry of Science and ICT [grant number RS-2023-00281246].

Data and materials availability

The data that support the findings of this study are available from the corresponding author upon reasonable request.

ORCID

Sujung Son http://orcid.org/0000-0003-3480-7331
Hyoung Seop Kim http://orcid.org/0000-0002-3155-583X

References

[1] Zhu Y, Ameyama K, Anderson PM, et al. Heterostructured materials: superior properties from hetero-zone interaction. Mater Res Lett. 2021;9(1):1–31.
[2] Sathiyamoorthi P, Kim HS. High-entropy alloys with heterogeneous microstructure: processing and mechanical properties. Prog Mater Sci. 2022;123:100709.
[3] Son S, Moon J, Kwon H, et al. Novel Co-Cu-based immiscible medium-entropy alloys with promising mechanical properties. Metals. 2021;11(2):238.
[4] Wu S, Wang G, Wang Q, et al. Enhancement of strength-ductility trade-off in a high-entropy alloy through a heterogeneous structure. Acta Mater. 2019;165:444–458.
[5] Vajpai SK, Ota M, Zhang Z, et al. Three-dimensionally gradient harmonic structure design: an integrated approach for high performance structural materials. Mater Res Lett. 2016;4(4):191–197.
[6] Kumaran M, Senthilkumar V, Sathies T, et al. Effect of heat treatment on stainless steel 316L alloy sandwich structure fabricated using directed energy deposition and powder bed fusion. Mater Lett. 2022;313:131766.
[7] Gu GH, Heo Y-U, Kwon H, et al. Synergy of tensile strength-ductility in IN718/CoCrFeMnNi/IN718 multi-material processed by powder high-pressure torsion and annealing. Scr Mater. 2023;225:115167.
[8] Eid M, Kaytbay S, El-Assal A, et al. Electrical, thermal, and mechanical characterization of hot coined carbon fiber reinforced pure aluminium composites. Met Mater Int. 2022;28:2747–2765.
[9] Suryanarayana C. Mechanical alloying and milling. Prog Mater Sci. 2001;46(1–2):1–184.
[10] Suprianto CC. Study of Cu effect and in-situ Yttria dispersoids on microstructure evolution of mechanically alloyed CoFeNiCrCu high entropy alloys. Met Mater Int. 2023;29:420–428.
[11] Asghari-Rad P, Sathiyamoorthi P, Nguyen NT-C, et al. A powder-metallurgy-based fabrication route towards achieving high tensile strength with ultra-high ductility in high-entropy alloy. Scr Mater. 2021;190:69–74.
[12] Son S, Asghari-Rad P, Zargaran A, et al. Superlative room temperature and cryogenic tensile properties of nanostructured CoCrFeNi medium-entropy alloy fabricated by powder high-pressure torsion. Scr Mater. 2022;213:114631.
[13] Hosseini Kahnooj SA, Vaseghi M, Sameezadeh M. Softening and microstructure evolution of pure copper disks processed by high pressure torsion. Met Mater Int. 2022;28:2646–2651.
[14] Edalati P, Mohammadi A, Ketabchi M, et al. Ultrahigh hardness in nanostructured dual-phase high-entropy

alloy AlCrFeCoNiNb developed by high-pressure torsion. J Alloy Compd. 2021;884:161101.
[15] Taheriniya S, Davani FA, Hilke S, et al. High entropy alloy nanocomposites produced by high pressure torsion. Acta Mater. 2021;208:116714.
[16] Akbarpour MR, Mirabad HM, Golenji RB, et al. Synergistic effects of MWCNTs and high-pressure torsion-induced grain refinement on microhardness, tribological properties, and corrosion behavior of Cu and Cu/MWCNT nanocomposites. Met Mater Int. 2022;28:2197–2215.
[17] Shafiei A, Rajabi S. A cobalt-rich eutectic high-entropy alloy in the system Al–Co–Cr–Fe–Ni. Appl Phys A. 2019;125(11):1–11.
[18] Reddy TS, Wani IS, Bhattacharjee T, et al. Severe plastic deformation driven nanostructure and phase evolution in a $Al_{0.5}CoCrFeMnNi$ dual phase high entropy. Intermetallics. 2017;91:150–157.
[19] Straumal BB, Baretzky B, Mazilkin AA, et al. Formation of nanograined structure and decomposition of supersaturated solid solution during high pressure torsion of Al–Zn and Al–Mg alloys. Acta Mater. 2004;52:4469–4478.
[20] Ivanisenko Y, Lojkowski W, Valiev RZ, et al. The mechanism of formation of nanostructure and dissolution of cementite in a pearlitic steel during high pressure torsion. Acta Mater. 2003;51(18):5555–5570.
[21] Zhang NX, Kawasaki M, Huang Y, et al. An examination of microstructural evolution in a Pb–Sn eutectic alloy processed by high-pressure torsion and subsequent self-annealing. Mater Sci Eng A. 2021;802:140653.
[22] Khalikova GR, Korznikova GF, Trifonov VG. Effect of structural-phase transformations on the microhardness of the Al-22%Si-3%Cu-1.7%Ni alloy after high-pressure torsion and annealing. IOP Conf Ser Mater Sci Eng. 2018;447:012073.
[23] Peranio N, Li YJ, Roters F, et al. Microstructure and texture evolution in dual-phase steels: competition between recovery, recrystallization, and phase transformation. Mater Sci Eng A. 2010;527:4161–4168.
[24] Wani IS, Bhattacharjee T, Sheikh S, et al. Cold-rolling and recrystallization textures of a nano-lamellar $AlCoCrFeNi_{2.1}$ eutectic high entropy alloy. Intermetallics. 2017;84:42–51.
[25] Bhattacharjee T, Zheng R, Chong Y, et al. Effect of low temperature on tensile properties of $AlCoCrFeNi_{2.1}$ eutectic high entropy alloy. Mater Chem Phys. 2018;210:207–212.
[26] Huo W, Fang F, Zhou H, et al. Remarkable strength of CoCrFeNi high-entropy alloy wires at cryogenic and elevated temperatures. Scr Mater. 2017;141:125–128.
[27] Zhang X, Wu P, Liang F, et al. Achieve high plasticity and strength in 6016 alloy by high-pressure torsion combined with post-aging treatments. J Mater Res Technol. 2023;22:2967–2982.
[28] Feng H, Cai L, Wang L. Microstructure and strength in ultrastrong cold-drawn medium carbon steel. J Mater Sci Technol. 2022;97:89–100.
[29] Zhao Z, Shen Z, Dong P, et al. Temperature-Dependent yield strength of nanoprecipitate-strengthened face-centered cubic high entropy alloys: prediction and analysis. Met Mater Int. 2022;29:1723–1738.
[30] Zheng F, Zhang G, Chen X, et al. A new strategy of tailoring strength and ductility of CoCrFeNi based high-entropy alloy. Mater Sci Eng A. 2020;774:138940.
[31] Rahul MR, Samal S, Venugopal S, et al. Experimental and finite element simulation studies on hot deformation behaviour of $AlCoCrFeNi_{2.1}$ eutectic high entropy alloy. J Alloy Compd. 2018;749:1115–1127.
[32] Wani IS, Bhattacharjee T, Sheikh S, et al. Tailoring nanostructures and mechanical properties of $AlCoCrFeNi_{2.1}$ eutectic high entropy alloy using thermo-mechanical processing. Mater Sci Eng A. 2016;675:99–109.
[33] Liu S, Chem Y, Yang H, et al. Revealing the role of heterostructural parameters in hetero-deformation induced stress of Mg–13Gd alloy. Mater Sci Eng A. 2022;839:142844.
[34] Bouaziz O, Kim HS, Lee J, et al. Bauschinger effect or kinematic hardening: bridging microstructure and continuum mechanics. Met Mater Int. 2023;29:280–292.
[35] Liu GF, Chen TJ. Effect of ball-milling process on microstructures and mechanical properties of heterostructured 2024Al alloy prepared by powder thixoforming. Met Mater Int. 2022;28:2919–2933.
[36] Zhao YH, Guo YZ, Wei Q, et al. Influence of specimen dimensions and strain measurement methods on tensile stress–strain curves. Mater Sci Eng A. 2009;525(1–2):68–77.
[37] Lee J, Bae JW, Asghari-Rad P, et al. Double-humped strain hardening in a metastable ferrous medium-entropy alloy by cryogenic pre-straining and subsequent heat treatment. Scr Mater. 2022;211:114511.
[38] Salishchev GA, Tikhonovsky MA, Shaysultanov DG, et al. Effect of Mn and V on structure and mechanical properties of high-entropy alloys based on CoCrFeNi system. J Alloy Compd. 2014;591:11–21.
[39] Liu WH, He JY, Huang HL, et al. Effects of Nb additions on the microstructure and mechanical property of CoCrFeNi high-entropy alloys. Intermetallics. 2015;60:1–8.
[40] Gali A, George EP. Tensile properties of high- and medium-entropy alloys. Intermetallics. 2013;39:74–78.
[41] He JY, Wang H, Huang HL, et al. A precipitation-hardened high-entropy alloy with outstanding tensile properties. Acta Mater. 2016;102:187–196.
[42] Liu WH, Lu ZP, He JY, et al. Ductile $CoCrFeNiMo_x$ high entropy alloys strengthened by hard intermetallic phases. Acta Mater. 2016;116:332–342.
[43] Huang T, Jiang L, Zhang C, et al. Effect of carbon addition on the microstructure and mechanical properties of CoCrFeNi high entropy alloy. Sci China Technol Sci. 2018;61:117–123.
[44] Liu H-C, Tsai C-W. Effect of Ge addition on the microstructure, mechanical properties, and corrosion behavior of CoCrFeNi high-entropy alloys. Intermetallics. 2021;132:107167.
[45] Chen X, Kong J, Li J, et al. High-strength $AlCoCrFeNi_{2.1}$ eutectic high entropy alloy with ultrafine lamella structure via additive manufacturing. Mater Sci Eng A. 2022;854:143816.
[46] Wang S, Li Y, Zhang D, et al. Microstructure and mechanical properties of high strength $AlCoCrFeNi_{2.1}$ eutectic high entropy alloy prepared by selective laser melting (SLM). Mater Lett. 2022;310:131511.

[47] Lu Y, Wu X, Fu Z, et al. Ductile and ultrahigh-strength eutectic high-entropy alloys by large-volume 3D printing. J Mater Sci Technol. 2022;126:15–21.
[48] He L, Wu S, Dong A, et al. Selective laser melting of dense and crack-free $AlCoCrFeNi_{2.1}$ eutectic high entropy alloy: synergizing strength and ductility. J Mater Sci Technol. 2022;117:133–145.
[49] Yang F, Wang L, Wang Z, et al. Ultra strong and ductile eutectic high entropy alloy fabricated by selective laser melting. J Mater Sci Technol. 2022;106:128–132.
[50] Dong B, Wang Z, Pan Z, et al. On the development of pseudo-eutectic $AlCoCrFeNi_{2.1}$ high entropy alloy using Powder-bed Arc Additive Manufacturing (PAAM) process. Mater Sci Eng A. 2021;802:140639.
[51] Huang L, Sun Y, Chen N, et al. Simultaneously enhanced strength-ductility of $AlCoCrFeNi_{2.1}$ eutectic high-entropy alloy via additive manufacturing. Mater Sci Eng A. 2022;830:142327.
[52] Gao X, Lu Y, Zhang B, et al. Microstructural origins of high strength and high ductility in an $AlCoCrFeNi_{2.1}$ eutectic high-entropy alloy. Acta Mater. 2017;141:59–66.
[53] Reddy SR, Sunkari U, Lozinko A, et al. Microstructural design by severe warm-rolling for tuning mechanical properties of $AlCoCrFeNi_{2.1}$ eutectic high entropy alloy. Intermetallics. 2019;114:106601.